

# Isolated and hybrid bilayer graphene rings

M. Mirzakhani<sup>1,2,\*</sup> and F. M. Peeters<sup>3,†</sup>

<sup>1</sup>*School of Physics, University of the Witwatersrand, Johannesburg, Wits 2050, South Africa*

<sup>2</sup>*Center for Theoretical Physics of Complex Systems,*

*Institute for Basic Science, Daejeon, 34126, South Korea*

<sup>3</sup>*Department of Physics, University of Antwerp, Groenenborgerlaan 171, B-2020 Antwerp, Belgium*

(Dated: February 28, 2023)

Using the continuum model, we investigate the electronic properties of two types of bilayer graphene ring (BLGR) geometries: (i) an isolated BLGR and (ii) a monolayer graphene (MLG) ring put on top of an infinite graphene sheet. Solving the Dirac-Weyl equation in the presence of a perpendicular magnetic field and applying infinite-mass boundary condition at the ring boundaries, we obtain analytical results for the energy levels and corresponding wave spinors for both structures. Our results show that the presence of interface boundary in a hybrid BLGR modifies drastically the energy levels as compared to that of an isolated BLGR. The intervalley symmetry  $E_e^K(m) = -E_h^{K'}(m)$  between the electron (e) and hole (h) states ( $m$  being the angular momentum quantum number) is found for the energy spectrum of an isolated BLGR, while it is broken for the hybrid BLGR. Our analytical results agree with those obtained within the tight-binding model (TBM). Sizeable and magnetically tunable band gap, in contrast to that in the zero-width BLGR model, is predicted for both ring structures, which experimentally can be measured in, e.g., magnetotransport measurements.

PACS numbers: 81.05.ue, 73.22.Pr, 73.20.-r, 68.65.-k

## I. INTRODUCTION

Over the past years, a family of two-dimensional (2D) graphene nanostructures, including graphene nanoribbons [1–6], rings [7–12], quantum dots (QDs) [13–25], and antidots [26–30] with different type of geometries, edge types, and stackings of graphene layers have received considerable interest. These studies showed that the electronic and optical properties of graphene QDs can be modified greatly by size, shape, edge type, and electrostatic gating; see, e.g., also Refs. [13, 16, 17, 20, 24]. The effect of twisting on the electronic and transport properties of bilayer graphene (BLG) nanostructures has also been recently addressed in Refs. [31–37]. Within today's technology, such as nanolithography, it is possible to realize such two-dimensional nanostructures on a scale of a few tens [38, 39] or even only a few [40, 41] nanometers as well as in different types of graphene layer stackings [42, 43].

Furthermore, bandstructure engineering can be performed by creating periodic arrays of holes in both MLG [27, 28, 30, 38] and BLG [44] sheets, known as graphene antidot lattices. Depending on the size and the period of the holes, such graphene nanostructures render graphene semiconducting with a sizeable band gap which displays a wide range of electronic and optical properties [44–46]. Very recently, a related system has been investigated where a MLG sheet consists of highly regular, triangularly arranged holes [30]. The results showed that the structure displays both insulating behaviour and ballistic

transport in excellent agreement with analytical calculations which describes the structure as a quantum system consisting of connected “Dirac rings” [30, 47]. In this model, Dirac fermions are strongly confined in a MLG ring geometry using an infinite-mass (IM) potential.

While in the case of MLG such holes can act as scattering centers, several experimental works [48, 49] demonstrated that in the case of BLG, the adjacent layers can connect with each other thus resulting in the formation of periodic arrays of connected *edgeless* Dirac rings in BLG structure. Theoretical study of such superlattices in BLG, consisting of hexagonal-ring arrays, showed that both semiconducting and metallic behaviors can be observed [44].

Here, we aim to investigate the electronic properties of such rings in BLG as an individual quantum ring defined by an IM potential. The latter has the advantage that analytical results can be obtained while still representing a real system [25]. Within this paper, we consider two types of BLGRs illustrated in Fig. 1: (a) an isolated BLGR and (b) a hybrid BLGR where a MLG ring is put on top of an infinite MLG sheet. The latter can be realized by nanostructuring one of the graphene layers in BLG. Topographic images have revealed that multilayer samples exfoliated from graphite often contain atomic steps and islands of one or few layers of graphene [50–54]. They have been previously investigated both theoretically and experimentally, in different configurations such as single MLG-BLG junction [55–61], double MLG-BLG junctions (MLG-BLG-MLG) [62, 63], and hybrid QD structures [64]. In all these studies the interface between MLG and BLG regions was considered as zigzag or armchair junctions which modify considerably the electronic properties of such structures.

\* mirzakhani@ibs.re.kr

† francois.peeters@uantwerpen.be

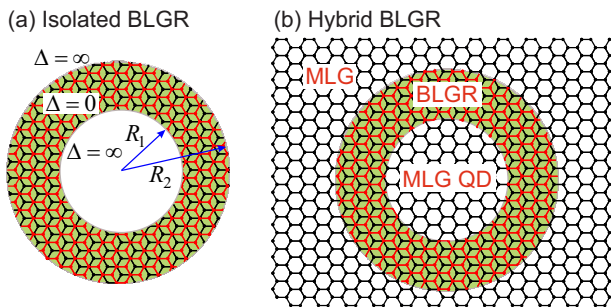


FIG. 1. Schematic pictures of the proposed circular BLGRs with inner and outer radii of  $R_1$  and  $R_2$ , respectively. (a) Isolated BLGR and (b) hybrid BLGR sandwiched between MLG QD and MLG sheet.

Theoretically, the IM boundary condition for confining neutrinos in a hard-wall billiard was derived by Berry and Modragon [65]. This boundary condition was previously employed to investigate the electronic properties of MLG nanostructures (dot, antidot, ring) [25, 29, 47, 66], BLG QDs [67], and trilayer graphene QDs [23]. Previous studies of BLGRs based on Dirac equation includes electrostatically defined BLGRs [68, 69] which was solved numerically in Ref. [68] and was modeled as zero-width-ring geometry in Ref. [69]. However, at present there is, to our knowledge, no theoretical study on the energy spectrum of BLGRs with IM boundary condition that models a realistic ring.

In the present work, we solve the Dirac-Weyl equation in the presence of a perpendicular magnetic field and apply the appropriate IM boundary condition at the ring boundaries to obtain analytical results for the energy levels and corresponding wave functions in both structures. Our results show that the energy spectrum of the isolated ring exhibits intervalley symmetry  $E_e^K(m) = -E_h^{K'}(m)$  for the electron (e) and hole (h) states, which is not the case for the hybrid ring. In addition, as a function of the magnetic field, the energy spectrum of both structures exhibits Aharonov-Bohm oscillations. We also investigate the dependence of the energy spectrum on the ring width for both structures.

To complement the study, we compare our analytical results with those obtained using TBM for small structures. We find good agreement between both approaches for the low energy levels in strong magnetic field. Furthermore, we analyze the valley- and layer-resolved local density of states (LDOS) for both proposed structures and our findings show that, at a given magnetic field, the contributions of the valleys as well as that of the layers in the LDOS can be different. This feature can be used in valleytronics applications of such graphene-based nanostructures if valley mixing is precluded.

## II. THEORY AND MODEL

We consider two different BLG nanostructures in the presence of a perpendicular magnetic field: (i) isolated BLGR [Fig. 1(a)] and (ii) hybrid BLGR sandwiched between a MLG QD and an infinite MLG region, as shown in Fig. 1(b). The latter one can also be regarded as an infinite MLG sheet on which a second MLG ring is sitting on top of the first, thus realizing a BLGR in the AB-stacking (Bernal) configuration. Dirac equation is solved for both MLG and BLG regions, with appropriate boundary conditions. By employing the IM boundary condition, we obtain analytical results for the energy levels and corresponding wave functions in each structure.

Experimentally, such a mass potential can be induced by sandwiching the BLG sheet between substrates such that the  $A$  and  $B$  sublattices in each graphene sheet feel different potentials [70, 71]. Equivalently, graphene nanostructures that are etched out of graphene sheets can be considered as strong confinement that can be modelled with IM-boundary condition.

In the presence of a perpendicular magnetic field  $\mathbf{B} = B\hat{e}_z$ , the dynamics of carriers in the honeycomb lattice of carbon atoms of MLG can be described by the following Hamiltonian [7],

$$\mathcal{H} = v_F \mathbf{\Pi} \cdot \boldsymbol{\sigma} + \Delta(\mathbf{r})\sigma_z, \quad (1)$$

where  $v_F \approx 10^6$  m/s is the Fermi velocity,  $\mathbf{\Pi} = \mathbf{p} + e\mathbf{A}$  is the two dimensional kinetic momentum operator with  $\mathbf{p} = -i\hbar(\partial_x, \partial_y)$ ,  $-e$  being the electron charge, and  $\mathbf{A} = (B/2)(-y\hat{e}_x + x\hat{e}_y)$  is the vector potential taken in the symmetric gauge.  $\boldsymbol{\sigma} = (\sigma_x, \sigma_y, \sigma_z)$  denotes the Pauli matrices and  $\Delta(\mathbf{r})$  is a position-dependent mass term. In polar coordinates  $(r, \varphi)$  the Hamiltonian (1) reduces to the form

$$\mathcal{H} = E_0 \begin{pmatrix} \delta & \Pi_- \\ \Pi_+ & -\delta \end{pmatrix}, \quad (2)$$

where  $E_0 = \sqrt{2}\hbar v_F/l_B$  is the cyclotron energy with  $l_B = \sqrt{\hbar/eB}$  the magnetic length,  $\delta = \Delta(\rho)/E_0$ , and the momentum operator

$$\Pi_{\pm} = \Pi_x \pm i\Pi_y = -ie^{\pm i\tau\varphi} \frac{1}{2} \left[ \frac{\partial}{\partial \rho} \pm \frac{i\tau}{\rho} \frac{\partial}{\partial \varphi} \mp \tau\rho \right]. \quad (3)$$

Here,  $\rho = r/\sqrt{2}l_B$  is a dimensionless radial coordinate and  $\tau = \pm 1$  distinguish the  $K$  and  $K'$  valleys. Because of circular symmetry, the two-component spinor wave function becomes  $\Psi^\tau(\rho, \varphi) = e^{im\varphi} [\phi_A^\tau(\rho), i\phi_B^\tau(\rho)e^{i\tau\varphi}]^T$  where the radial dependence of the spinor components is described by

$$\begin{aligned} \frac{1}{2} \left[ \frac{\partial}{\partial \rho} + \frac{(\tau m + 1)}{\rho} + \tau\rho \right] \phi_B^\tau(\rho) &= (\epsilon - \delta)\phi_A^\tau(\rho), \\ \frac{1}{2} \left[ \frac{\partial}{\partial \rho} - \frac{\tau m}{\rho} - \tau\rho \right] \phi_A^\tau(\rho) &= -(\epsilon + \delta)\phi_B^\tau(\rho), \end{aligned} \quad (4)$$

where  $m = 0, \pm 1, \pm 2, \dots$  denotes the angular momentum label and  $\epsilon = E/E_0$  being the dimensionless carrier energy. Decoupling the above equations and using the ansatz for  $\phi_A^\tau(\rho) = \rho^{-m} e^{-\rho^2/2} f(\rho^2)$ , one arrives at the associated Laguerre differential equation ( $\tilde{\rho} = \rho^2$ )

$$\tilde{\rho} f''(\tilde{\rho}) + (-m + 1 - \tilde{\rho}) f'(\tilde{\rho}) + \lambda f(\tilde{\rho}) = 0, \quad (5)$$

where

$$\lambda = \frac{1}{2}[-(\tau + 1) + 2(\epsilon^2 - \delta^2)]. \quad (6)$$

The general solution to the associated Eq. (5) is

$$f(\rho^2) = C_1 L_\lambda^{-m}(\rho^2) + C_2 U(-\lambda, 1 - m, \rho^2), \quad (7)$$

where the constants  $C_1$  and  $C_2$  are determined by the boundary conditions.  $U(a, b, x)$  is the *confluent hypergeometric function of the second kind* and  $L_a^b(x)$  is the *generalized Laguerre polynomial* which can be defined in terms of the confluent hypergeometric function of the first kind  $M(a, b, x)$  [the other notation is  ${}_1F_1(a, b, x)$ ] as

$$L_a^b(x) = \binom{a+b}{a} M(-a, b+1, x), \quad (8)$$

where  $\binom{a+b}{a}$  is a generalized binomial coefficient.

Notice that  $\rho^{-m} e^{-\rho^2/2} L_\lambda^{-m}(\rho)$  and  $\rho^{-m} e^{-\rho^2/2} U(-\lambda, 1 - m, \rho)$  converge to finite values in the limits  $\rho \rightarrow 0$  and  $\rho \rightarrow \infty$ , respectively. So, depending on the geometry of the graphene nanostructures (dot or antidot), one can choose the appropriate wave functions to satisfy the corresponding boundary conditions.

The other spinor component of the wave function,  $\phi_B^\tau(\rho)$ , can be obtained using Eq. (4) and by employing the properties of  $U(a, b, x)$  and  $L_a^b(x)$ . Thus the spinor components become

$$\phi_A^\tau(\rho) = \rho^{-m} e^{-\rho^2/2} \times \left[ C_1 L_\lambda^{-m}(\rho^2) + C_2 U(-\lambda, 1 - m, \rho^2) \right], \quad (9)$$

and

$$\phi_B^\tau(\rho) = \frac{-\tau}{\epsilon + \delta} \rho^{-m-\tau} e^{-\rho^2/2} \left[ C_1 (\lambda + \tau_+)^{\tau_+} L_{\lambda+\tau_+}^{-m-\tau}(\rho^2) - C_2 (\lambda + \tau_+)^{\tau_-} U(-\lambda - \tau, -m + 1 - \tau, \rho^2) \right], \quad (10)$$

where we have defined  $\tau_\pm = (1 \pm \tau)/2$ .

The BLG region can be described in terms of four sublattices, labeled  $A1, B1$ , for the lower layer and  $A2, B2$ , for the upper layer. We only include the coupling between two atoms stacked on top of each other, e.g.,  $B1$

and  $A2$ , and ignore the small contributions of the other interlayer couplings. The effective Hamiltonian is [72, 73]

$$\mathcal{H}_B = E_0 \begin{pmatrix} \delta & \Pi_- & 0 & 0 \\ \Pi_+ & -\delta & \tilde{\gamma}_1 & 0 \\ 0 & \tilde{\gamma}_1 & \delta & \Pi_- \\ 0 & 0 & \Pi_+ & -\delta \end{pmatrix}, \quad (11)$$

where  $\tilde{\gamma}_1 = \gamma_1/E_0$  with  $\gamma_1 \approx 0.4$  eV being the nearest-neighbor interlayer coupling term. Solving the Dirac equation  $\mathcal{H}_B \Phi = E \Phi$  for the four-component wave function

$$\Phi^\tau(r, \varphi) = e^{i m \varphi} \times \left[ e^{-i \tau \varphi} \phi_{A1}(\rho), i \phi_{B1}(\rho), i \phi_{A2}(\rho), e^{i \tau \varphi} \phi_{B2}(\rho) \right]^T, \quad (12)$$

the radial dependence of the spinor components in BLG are described by

$$\begin{aligned} \frac{1}{2} \left[ \frac{d}{d\rho} + \frac{\tau m}{\rho} + \tau \rho \right] \phi_{B1}^\tau(\rho) &= (\epsilon - \delta) \phi_{A1}^\tau(\rho), \\ \frac{1}{2} \left[ \frac{d}{d\rho} - \frac{\tau m - 1}{\rho} - \tau \rho \right] \phi_{A1}^\tau(\rho) - \tilde{\gamma}_1 \phi_{A2}^\tau(\rho) &= -(\epsilon + \delta) \phi_{B1}^\tau(\rho), \\ \frac{1}{2} \left[ \frac{d}{d\rho} + \frac{\tau m + 1}{\rho} + \tau \rho \right] \phi_{B2}^\tau(\rho) - \tilde{\gamma}_1 \phi_{B1}^\tau(\rho) &= -(\epsilon - \delta) \phi_{A2}^\tau(\rho), \\ \frac{1}{2} \left[ \frac{d}{d\rho} - \frac{\tau m}{\rho} - \tau \rho \right] \phi_{A2}^\tau(\rho) &= (\epsilon + \delta) \phi_{B2}^\tau(\rho). \end{aligned} \quad (13)$$

Decoupling the system of equations (13) and using  $\phi_{A2}^\tau(\rho) = \rho^{-m} e^{-\rho^2/2} g(\rho^2)$ , we arrive at the following associated Laguerre differential equation ( $\tilde{\rho} = \rho^2$ )

$$\tilde{\rho} g''(\tilde{\rho}) + (-m + 1 - \tilde{\rho}) g'(\tilde{\rho}) + \alpha_\pm(\epsilon) g(\tilde{\rho}) = 0, \quad (14)$$

where  $\alpha_\pm(\epsilon)$  is given by

$$\alpha_\pm(\epsilon) = \frac{1}{2} \left[ 2(\epsilon^2 - \delta^2) - 1 \pm \sqrt{1 + 4\tilde{\gamma}^2(\epsilon^2 - \delta^2)} \right]. \quad (15)$$

Accordingly, similar to the MLG region,  $\phi_{A2}^\tau(\rho)$  can be expressed in terms of  $L_a^b(x)$  and  $U(a, b, x)$  as follows:

$$\phi_{A2}^\tau(\rho) = \rho^{-m} e^{-\rho^2/2} \times \sum_{\mu=\pm} \left[ C_1^\mu L_{\alpha_\mu}^{-m}(\rho^2) + C_2^\mu U(-\alpha_\mu, 1 - m, \rho^2) \right], \quad (16)$$

where the constants  $C_1^\mu$  and  $C_2^\mu$  are determined by the boundary conditions. The other spinor components of the wave function can be obtained using Eqs. (13) by inserting  $\phi_{A2}^\tau(\rho)$  and employing the properties of  $U(a, b, x)$  and  $L_a^b(x)$  functions. It is possible to express the other components in a compact form as follow:

$$\begin{aligned}
\phi_{A1}^\tau(\rho) &= \frac{-\tau \rho^{-m+\tau} e^{-\rho^2/2}}{\tilde{\gamma}_1(\epsilon^2 - \delta^2)} \sum_{\mu=\pm} \eta_\mu \left[ C_1^\mu (\alpha_\mu + \tau_-)^{\tau-} L_{\alpha_\mu - \tau}^{-m+\tau}(\rho^2) - C_2^\mu (\alpha_\mu + \tau_-)^{\tau+} U(-\alpha_\mu + \tau, -m + 1 + \tau, \rho^2) \right], \\
\phi_{B1}^\tau(\rho) &= \frac{\rho^{-m} e^{-\rho^2/2}}{\tilde{\gamma}_1(\epsilon + \delta)} \sum_{\mu=\pm} \eta_\mu \left[ C_1^\mu L_{\alpha_\mu}^{-m}(\rho^2) + C_2^\mu U(-\alpha_\mu, -m + 1, \rho^2) \right], \\
\phi_{B2}^\tau(\rho) &= \frac{\tau \rho^{-m-\tau} e^{-\rho^2/2}}{\epsilon + \delta} \sum_{\mu=\pm} \left[ C_1^\mu (\alpha_\mu + \tau_+)^{\tau+} L_{\alpha_\mu + \tau}^{-m-\tau}(\rho^2) - C_2^\mu (\alpha_\mu + \tau_+)^{\tau-} U(-\alpha_\mu - \tau, -m + 1 - \tau, \rho^2) \right], \quad (17)
\end{aligned}$$

where  $\eta_\mu = [\epsilon^2 - \delta^2 - (\alpha_\mu + \tau_\pm)]$ .

Berry and Modragon derived the IM boundary condition for the confinement of neutrinos in a hard-wall billiard described by the Dirac-Weyl equation [65]. Lets consider a particle restricted in the plane  $\mathbf{r} = (x, y)$  subjected to a mass term potential  $\Delta(\mathbf{r})$ , which is vanishing inside a certain domain and equal to  $\Delta \rightarrow \infty$  outside it. Solving the Dirac equation, Eq. (1), for a two-component spinor  $[\psi_1(\mathbf{r}), \psi_2(\mathbf{r})]^T$  leads to the following relation at the domain edge [65]

$$\psi_2(\mathbf{r})/\psi_1(\mathbf{r}) = i e^{i\tau\theta}, \quad (18)$$

where  $\theta$  is the polar angle of the normal vector points outward from the domain boundary. Within the next section, we will calculate the energy spectrum of both ring structures using the above-mentioned boundary condition.

### III. NUMERICAL RESULTS

In the case of isolated BLGR, applying the IM boundary condition (18) for each layer, the spinor components at the radial distances  $R_1$  ( $\theta = \pi + \varphi$ ) and  $R_2$  ( $\theta = \varphi$ ) satisfy the conditions

$$\begin{aligned}
\phi_{B1}^\tau(\rho_1) + \phi_{A1}^\tau(\rho_1) &= 0, \\
\phi_{B2}^\tau(\rho_1) - \phi_{A2}^\tau(\rho_1) &= 0 \quad (19)
\end{aligned}$$

and

$$\begin{aligned}
\phi_{B1}^\tau(\rho_2) - \phi_{A1}^\tau(\rho_2) &= 0, \\
\phi_{B2}^\tau(\rho_2) + \phi_{A2}^\tau(\rho_2) &= 0, \quad (20)
\end{aligned}$$

respectively, with  $\rho_i = R_i/\sqrt{2}l_B$  ( $i = 1, 2$ ). The eigenvalue condition is determined by inserting the obtained spinors for BLG, Eqs. (16) and (17), with  $\delta = 0$  into the above four equations. Note that the effect of IM potential  $\Delta \rightarrow \infty$  is now expressed by the boundary conditions (19) and (20).

For the hybrid BLGR, the spinors corresponding to the sublattices in the lower layer are continuous at the ring boundaries, while the spinor components of the upper (ring) layer,  $\phi_{A2}^\tau(\rho)$  and  $\phi_{B2}^\tau(\rho)$ , satisfy the IM boundary

condition expressed by Eqs. (19) and (20). Thus, in this case, the boundary conditions at  $R_{1(2)}$  read

$$\begin{aligned}
\phi_A^\tau(\rho_{1(2)}) - \phi_{A1}^\tau(\rho_{1(2)}) &= 0, \\
\phi_B^\tau(\rho_{1(2)}) - \phi_{B1}^\tau(\rho_{1(2)}) &= 0, \\
\phi_{B2}^\tau(\rho_{1(2)}) \mp \phi_{A2}^\tau(\rho_{1(2)}) &= 0. \quad (21)
\end{aligned}$$

where  $-(+)$  is used at  $R_{1(2)}$  boundary.

Here, we have to stress two points: First, using the above boundary conditions when implementing them numerically gives two sets of energy levels. A set of levels corresponds to the pristine BLG Landau levels (LLs), which mathematically originates from the proportionality of  $L_a^b(x)$  and  $U(a, b, x)$  functions when  $a$  ( $\equiv \alpha_\pm(\epsilon)$ ) becomes an integer number  $n$ . In this case,  $L_n^b(x) = \frac{(-1)^n}{n!} U(-n, b + 1, x)$  and the wave spinors become finite in both limits  $r \rightarrow 0$  and  $\infty$  as for bulk BLG LLs [57]. Second, our calculations show that the energy spectrum of the isolated ring exhibits the intervalley symmetry  $E^K(m) = -E^{K'}(m)$ . Due to this connection between the valleys, we only consider the energy spectrum of one valley, e.g.,  $K$  valley. For the hybrid ring, the  $K$  and  $K'$  valleys are studied separately because of the lack of inversion symmetry brought by the interfaces.

The energy spectrum of an isolated BLGR, as a function of magnetic field, is shown in Fig. 2(a) for several values of the angular momenta,  $m = \pm 10$ ,  $m = \pm 2$ ,  $m = \pm 1$ , and  $m = 0$  at the  $K$  valley. The inner and outer ring radii, respectively, are  $R_1 = 30$  nm and  $R_2 = 40$  nm. For a single valley, as seen in panel (a), two broken symmetries are clearly visible in the presence of the magnetic field: (i) For a specific angular momentum  $m$ , the electron-hole (e-h) symmetry is broken, i.e.,  $E_e(m) \neq -E_h(m)$  and (ii)  $E(m) \neq E(-m)$ , since time reversal symmetry (TRS) is broken by the magnetic field [7]. Both symmetries are restored at  $B = 0$  as expected, because TRS is present when  $B = 0$ . For large field strength, the magnetic-field dependence of the spectrum becomes approximately linear which was also observed for the MLG ring and antidot spectra [47]. Note that, as function of the magnetic field, the lowest electron and hole energy levels show a ‘‘Mexican-hat’’ shape similar as the Mexican-hat-shaped low-energy dispersion for a biased AB-stacked BLG [74]. This behavior is more noticeable for large  $|m|$  as seen for  $m = -10$  in Fig. 2(a).

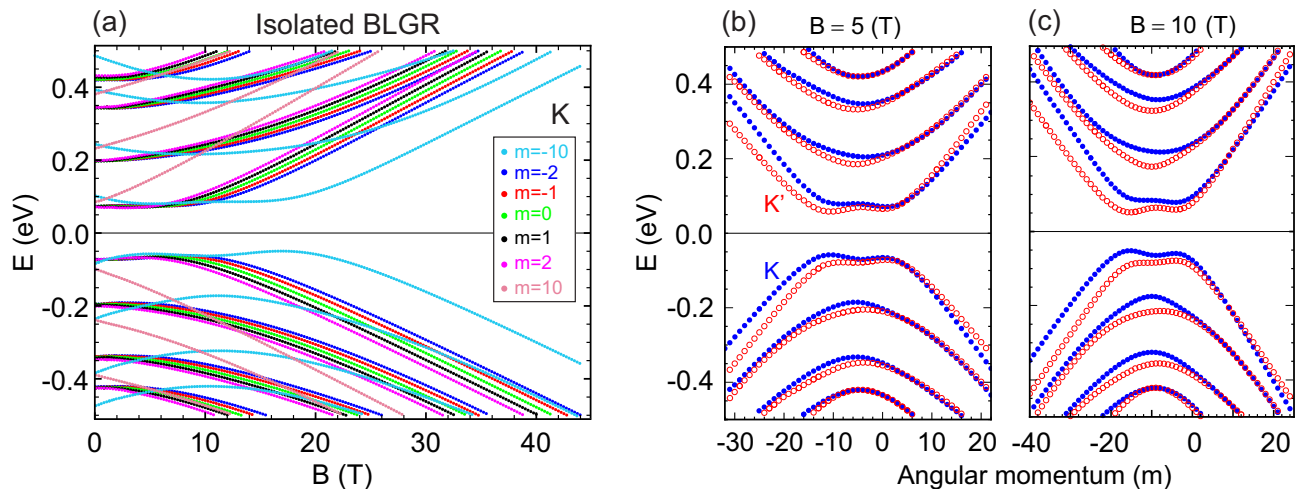


FIG. 2. (a) Energy spectrum of an isolated BLGR in the  $K$  valley as a function of the magnetic field  $B$ , with inner and outer radii  $R_1 = 30$  nm and  $R_2 = 40$  nm. The results are plotted for several angular momenta  $m = \pm 10, \pm 2, \pm 1, 0$ . (b,c) Energy levels of the same ring as a function of the angular momentum  $m$  in the  $K$  (full blue circles) and  $K'$  (open red circles) valleys for two different magnetic fields (b)  $B = 5$  T and (c)  $B = 10$  T. The symmetry  $E_e^K(m) = -E_h^{K'}(m)$  is clearly visible.

Including the energy levels of both valleys [see Fig. 6(b)] we can see that the confinement-induced band gap closes with increasing magnetic field. This is in contrast with the previous study of the zero-width BLGR [69], which shows a constant energy band gap as a function of the magnetic field.

In Figs. 2(b) and 2(c), the energy spectrum of both valleys is shown as a function of the angular momentum  $m$ . The results are presented for two different magnetic fields (b)  $B = 5$  T and (c)  $B = 10$  T with full blue (open red) circles for the  $K$  ( $K'$ ) valley. Irrespective of the magnetic-field strength, the energy spectra exhibit intervalley symmetry  $E_e^K(m) = -E_h^{K'}(m)$  between the electron and hole states, indicating that valley degeneracy is lifted. Lifting the valley degeneracy, due to the presence of the magnetic field, has also been noticed before in other graphene nanostructures [7, 23, 67], and is of great interest because it could make them promising candidates for *valleytronics* applications. One can see that decreasing the field  $B$ , suppresses the above-mentioned intervalley symmetry and the valley degeneracy is restored at  $B = 0$  [cf. Figs. 2(b) and 2(c)]. In the case of zero-width BLGR [69], the energy spectrum shows only two energy levels for each  $m$ , and the spectrum versus  $m$  is very similar to the band structure of a biased BLG sheet (see Fig. 10 in Ref. [69]). However, here, we find several energy levels as a function of  $m$  and the numbers depend on the width of the ring.

Results for the spectrum of a hybrid BLGR, of radius  $R_1 = 30$  nm and  $R_2 = 40$  nm, as a function of the magnetic field  $B$  at both valleys  $K$  and  $K'$  are shown in Figs. 3(a) and 3(b), respectively. The angular momenta are  $m = -1$  (blue),  $m = 0$  (green), and  $m = 1$  (red). This  $B$ -field dependence of the hybrid BLGR energy spectra is strikingly different from that of the isolated BLGR.

Here, for  $B = 0$ , the spectrum is continuous because of the presence of the infinite MLG, and with increasing magnetic field the degeneracy of the states is removed. The discrete levels (reflecting the confined states) depend on the angular momentum and the  $B$ -field strength. The spectra for both valleys show anticrossings, which is due to the influence of the MLG dot and BLGR interface. As a result of this interface, the symmetry condition  $E_e^K(m) = -E_h^{K'}(m)$  (which holds for an isolated ring) is no longer preserved here, as shown explicitly in Fig. 3(c). At high magnetic fields, i.e.,  $l_B < R_1$ , the energy levels merge into the LLs of pristine MLG ( $E_n = \pm\sqrt{2}n\hbar v_F/l_B$  with  $n = 0, 1, \dots$ , dashed black curves) indicating that magnetically confinement dominates and the carriers become localized at the center of the dot region (see Fig. 4 and the corresponding discussion). It is also worth noting that, here, the states with  $m < 0$  contributes to the zero LL ( $n = 0$ ) only in one valley ( $K$ ). This is in contrast with the other graphene nanostructures such as MLG [25] and BLG QDs [67] with IM boundary condition in which the states from both valleys form the zero LL.

As a function of the angular momentum, the energy spectrum is shown in Fig. 3(c) for a specific magnetic field ( $B = 10$  T) at the valleys  $K$  (full blue circles) and  $K'$  (open red circles). As seen, there is no symmetry between the e-h energies as well as those of valleys. For a given magnetic field, the energy levels at both valleys are affected by the ring interface for a particular range of  $m$  and converge to the MLG LLs for larger  $m$ 's (green lines), indicating carrier localization inside the dot region. Note that at the  $K$  ( $K'$ ) valley, the maximum value of the angular momentum  $m_{\max}$  that is converged to the  $n$ th electron LL of MLG is  $m_{\max} = n - 1$  ( $m_{\max} = n$ ,  $n \neq 0$ ). Further, in both valleys, the electron states show a smooth oscillatory behavior as function of

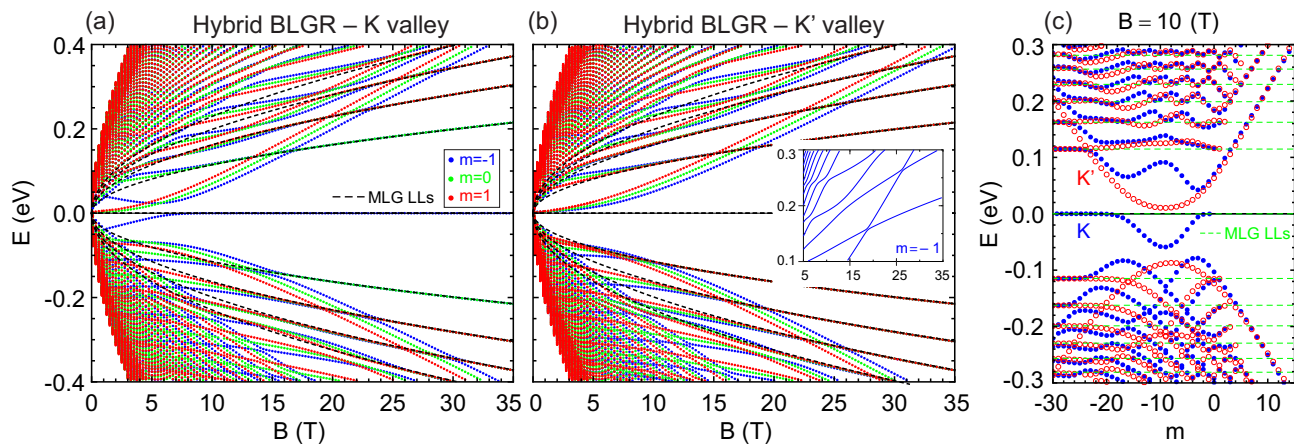


FIG. 3. Energy spectrum of a hybrid BLGR as a function of magnetic field  $B$ , with inner and outer radii  $R_1 = 30$  nm and  $R_2 = 40$  nm in the (a)  $K$  and (b)  $K'$  valleys. The results are plotted for three different angular momenta  $m = \pm 1, 0$ . The dashed black curves show the Landau levels ( $n = 0, 1, \dots, 4$ ) of pristine MLG sheet. The inset in panel (b) shows an enlarged view of the spectrum, showing the anticrossings for angular momentum  $m = 1$  and the  $K'$  valley. (c) Energy levels as a function of the angular momentum  $m$  for the same hybrid ring at  $B = 10$  T for two valleys  $K$  (full blue circles) and  $K'$  (open red circles). The dashed green lines pertain to the bulk MLG LLs at  $B = 10$  T for  $n = 0, 1, \dots, 6$ .

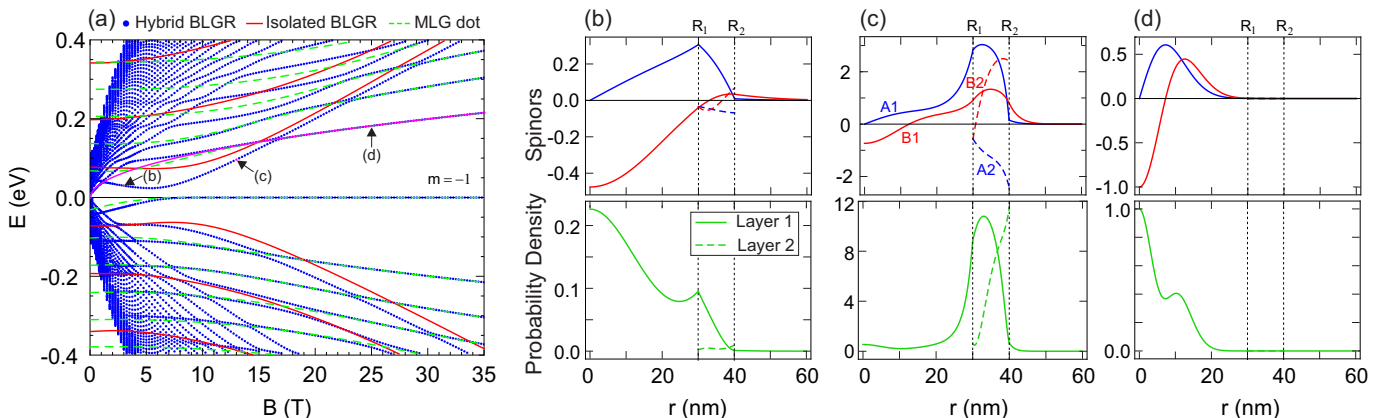


FIG. 4. (a) Lowest energy levels of a hybrid BLGR (blue circles), isolated BLGR (red curves), and MLG dot (dashed green curves) as a function of the magnetic field  $B$ , for angular momentum,  $m = -1$  in the  $K$  valley. The rings radii are  $R_1 = 30$  nm and  $R_2 = 40$  nm and the radius of the MLG dot is  $R_1 = 30$  nm. The magenta curve indicates the first electron LL ( $n = 1$ ) of MLG sheet. Panels (b), (c), and (d) are the wave spinors (upper panels) and probability densities (lower panels) corresponding to, respectively, the states labeled by (b), (c), and (d) in the energy spectrum of panel (a). Layer 1 (2) is represented by the solid (dashed) curves. Sublattices  $A_i$ , ( $B_i$ ) are represented by blue (red) curves.

magnetic field and strong anticrossings are visible also for hole states. Similar behavior was also noted for the double MLG-BLG junctions studied in Ref. [63] when the spectra are plotted as a function of the center coordinate of the cyclotron orbit.

To better understand the behavior of the energy levels in the spectrum of the hybrid ring, we plot, in Fig. 4, the energy levels of both types of rings and MLG dot for a specific angular momentum,  $m = -1$  [panel (a)], as well as the corresponding spinor components [ $\phi_\nu(\rho)$ ,  $\nu = A, B, \dots$ ] and probability densities [ $\phi_A^2(\rho) + \phi_B^2(\rho), \dots$ ] for the representative energy states marked by (b), (c), and (d) in Fig. 4(a), [panels (b)-(d)]. As seen, the energy levels of the hybrid ring seem to *interplay* between

the MLG dot, isolated BLGR, and MLG Landau energy levels as  $B$  increases. At the representative state (b), the energy level (blue circles) resembles that of the MLG dot (dashed green curves), the corresponding quantum state is mostly confined inside the dot region with a substantial probability density in the ring region, see (b) panels. When the energy level approaches the one of the isolated ring (red curves), e.g., point (c), the carrier is mostly confined inside the ring region [Fig. 4(c)]. For strong magnetic field, e.g., point (d), the energy level converges to the MLG LL (magenta curve), the state is completely confined inside the dot region, as seen in Fig. 4(d).

It is also interesting to investigate the effect of ring width on the energy spectrum of both structures. For

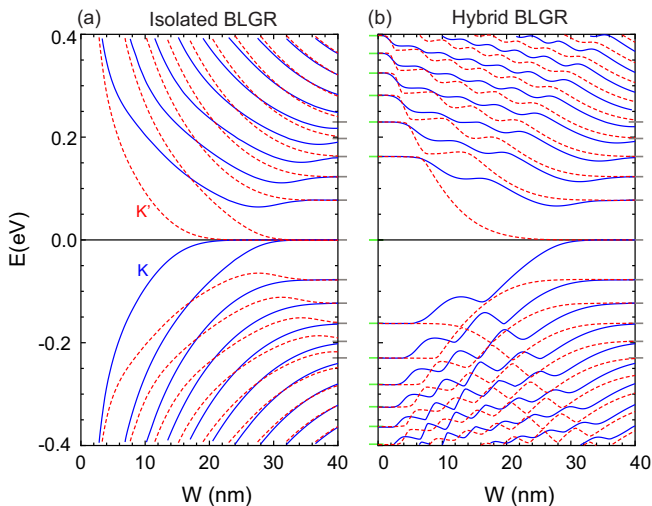


FIG. 5. Energy levels of (a) isolated and (b) hybrid rings as a function of ring width  $W$ , for angular momentum  $m = -20$  at the two valleys  $K$  (solid) and  $K'$  (dashed) when  $B = 20$  T. In both cases, the inner radius of the ring is  $R_1 = 20$  nm and the outer one  $R_2 = R_1 + W$ . The solid green and gray lines indicate, respectively, the bulk MLG and BLG LLs at  $B = 20$  T.

this purpose, we plot in Fig. 5 the lowest energy levels as a function of the width of the ring  $W (= R_2 - R_1)$  for (a) isolated and (b) hybrid BLGRs. In both cases, for the sake of clarity, the results are presented only for particular angular momentum  $m = -20$  at  $B = 20$  T. In the case of an isolated ring, the energy levels are separated by a gap, depending on the angular momentum and ring width, which closes when  $W$  increases and the energy levels for both valleys approach the LLs of bulk BLG as depicted by the horizontal gray lines. In the hybrid ring, Fig. 5(b), at small ring widths, the energy levels correspond to the LLs of MLG. When  $W$  increases, the electron (hole) energy levels, due to the influence of MLG-BLG interface, exhibit a flat plateau (strong anti-crossing) features for certain ranges of  $W$ , and eventually merge into the LLs of bulk BLG. The plateau-like and oscillatory features appearing in the energy spectrum can be understood as hybridization of the energy levels of the terminated systems, MLG QD and BLG antidot. Similar behavior was found for previous studies of MLG-BLG junctions [57, 63, 64].

In order to check the validity of the continuum approximation, we compare our analytical results with the energy levels calculated within a nearest-neighbor tight-binding approach. We include only the nearest-neighbor hopping parameters  $\gamma_0 = -2.7$  eV and  $\gamma_1 = 0.4$  eV as *intralayer* and *interlayer* couplings, respectively. The effect of an external magnetic field can be introduced into the calculations via the Peierls substitution  $t_{ij} \rightarrow t_{ij} e^{i2\pi\Phi_{ij}}$  where  $\Phi_{ij} = (1/\Phi_0) \int_{\mathbf{R}_i}^{\mathbf{R}_j} \mathbf{A}(\mathbf{r}) \cdot d\mathbf{r}$  is the Peierls phase [75] with  $\Phi_0 = h/e \approx 4.14 \times 10^{-15}$  Wb the magnetic flux quantum and  $\mathbf{A}(\mathbf{r}) = (0, Bx, 0)$  the vector

potential in the Landau gauge. Here, the quantum rings are defined by a staggered site-dependent potential such that the atoms belonging to the sublattices  $A1$  ( $A2$ ) and  $B1$  ( $B2$ ) have a mass-term potential of  $+M_0$  ( $+M_0$ ) and  $-M_0$  ( $-M_0$ ), respectively, as shown in Fig. 6(a). This simulates the substrate effect and can be regarded as the IM boundary condition in the TBM. More details of the geometries are provided in the caption of Fig. 6. Furthermore, our calculations show that in the Dirac model, applying the same radius used to define the atomic geometries in TBM, results in the energy levels which are slightly larger than those obtained by TBM. Two possible explanations for this discrepancy can be considered. First, in the TBM to simulate the IM boundary, we have used a narrow ribbon of  $\Delta r$  containing atoms with different on-site potentials in addition to the ring radii as shown in Fig. 6(a). The second which has also been proposed in Ref. [76], can be attributed to the  $\pi$  electrons that in the TBM extend over the real geometry. Accordingly, to compensate for this difference, we use a larger width for the rings in the Dirac model.

In Figs. 6(b) and 6(c), we compare the results obtained within the TB and Dirac approaches for the lowest-energy levels of both rings as a function of magnetic field  $B$ , see the figure caption for details. Notice that the Dirac results agree with the TB ones, especially for the lower-energy states. In the case of an isolated ring, there are some discrepancies between the two models for the hole energy levels. This is due to the fact that in the TBM, applying IM boundary at the edge boundary which is now not a perfect circle, breaks the e-h symmetry. This symmetry, however, is preserved in the Dirac model as a result of its perfect circular geometry. Moreover, in the TBM results of the hybrid ring [solid blue curves in Fig. 6(c)], we see a bunch of energy levels decreasing in energy and approaching the zero energy. They are known as the quantum *Hall* edge states [77] and are confined at the edges of the graphene flakes and are a result of the finite size of the flake. These Hall edge states are absent in the Dirac model for which the first layer is considered as an infinite graphene sheet. In general, we expect good agreement between the Dirac and TB models for the low-energy states. For the higher energy levels and high magnetic field, discrepancy between the Dirac and TB results becomes more significant. The reason is that the linear spectrum invoked in the Dirac equation is no longer valid.

We also notice that the energy spectra in both cases, exhibit periodic oscillations as the magnetic flux varies. This is a direct consequence of the Aharonov-Bohm (AB) effect [78] which is well known and has been investigated for quantum rings (metallic, semiconductor as well as graphene) [8, 79–82]. Similar to the AB effect in semiconductor quantum rings, the energy oscillations manifest itself in AB oscillations in the persistent current  $j(\Phi) = -\frac{\partial}{\partial \Phi} E$ .

Finally, we consider the valley- and layer-resolved LDOS for the studied structures which can be probed

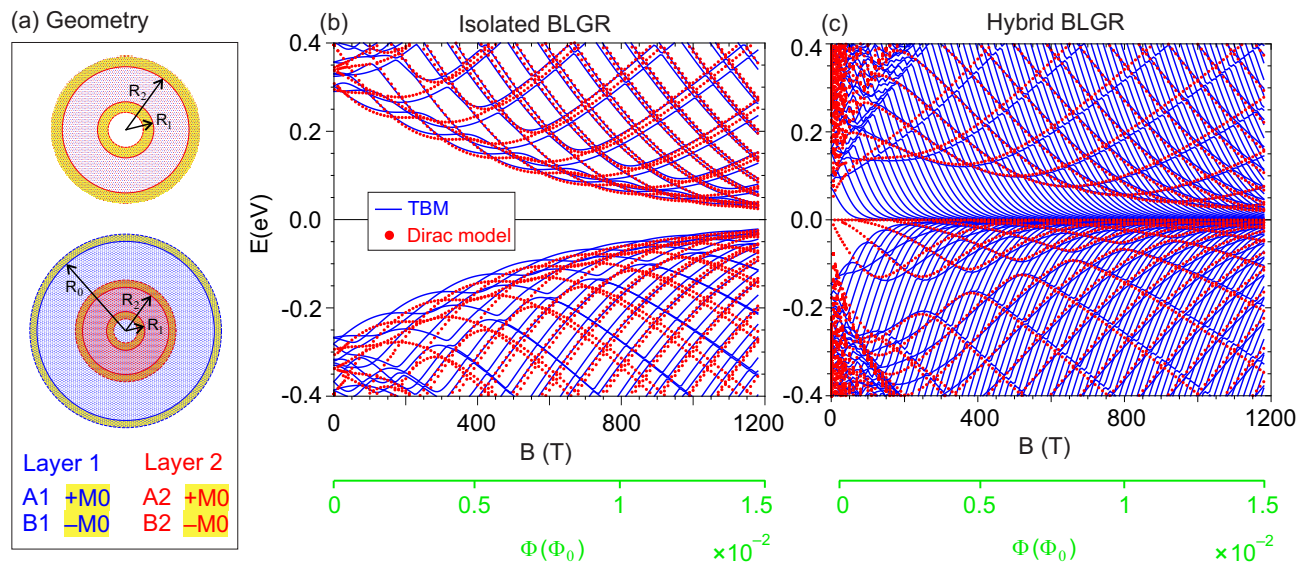


FIG. 6. (a) Schematic geometry of the circular BLGRs with inner and outer radii of  $R_1$  and  $R_2$  defined by the IM boundary used in TBM simulation. The upper (lower) panel depicts the isolated (hybrid) BLGR geometry. The atoms of the two layers are represented by blue (layer 1) and red (layer 2) circles. The ring regions are surrounded by a site-dependent staggered potential (yellow areas), where the atoms belonging to the sublattices A1 (A2) and B1 (B2) have mass-term potentials of  $+M_0$  ( $+M_0$ ) and  $-M_0$  ( $-M_0$ ), respectively. In the case of hybrid ring, to simulate the lower layer as an infinite graphene sheet, we consider it as a large circular flake (layer 1) on which a second MLG ring (layer 2) is sitting on top of it. Further, to eliminate the specific edge effects of layer 1, here also, we apply the staggered potential on the atoms located within the ribbon width of  $\Delta r = 2a_0$  ( $a_0 = 0.246$  nm being the lattice constant of graphene) at the edge of the flake (yellow region). (b,c) Energy levels of (b) an isolated BLGR and (c) a hybrid BLGR as function of the magnetic field  $B$ , calculated within the Dirac (red circles) and the TB (solid blue curves) models. For both cases, the results are presented for rings with inner and outer radii of  $R_1 = 8a_0 = 1.97$  nm and  $R_2 = 18a_0 = 4.43$  nm. The mass potential is  $M_0 = 2$  eV. In the hybrid ring, we use a circular flake of radius  $R_0 = 38a_0 = 9.35$  nm for the lower layer.

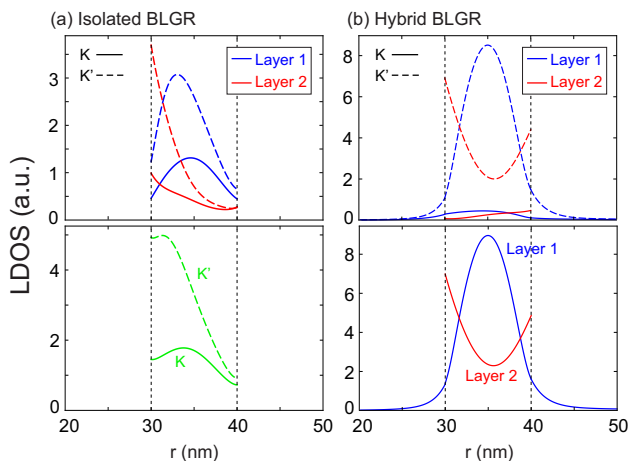


FIG. 7. Valley- and layer-resolved local density of states [LDOS (arbitrary units)] of (a) an isolated BLGR and (b) a hybrid BLGR with the inner and outer radii of  $R_1 = 30$  nm and  $R_2 = 40$  nm, respectively. The magnetic field is  $B = 10$  (T). Layer 1 (2) is represented by the blue (red) curves. The solid (dashed) curves correspond to the  $K$  ( $K'$ ) valley. For the isolated BLGR, the LDOS is computed in the energy range of  $[0, 0.2]$  eV, while for the hybrid one, the states in the energy window of  $[0, 0.11]$  eV [states between the lowest MLG LLs,  $n = 0$  and  $n = 1$  in Fig. 3(c)] are sampled.

by quantum capacitance measurements and by scanning tunneling microscopy. We consider the LDOS in the energy window of  $\Omega \equiv [E_1, E_2]$  which can be obtained using

$$\rho_{\ell}^{\tau}(r) = \sum_{E_i \in \Omega} \delta(E - E_i) |\psi_{\ell}^{E_i}(r)|^2, \quad (22)$$

where  $\psi_{\ell}^{E_i}(r) = [\phi_{A\ell}^{E_i}(r), \phi_{B\ell}^{E_i}(r)]^T$  denotes the quantum state of the two layers ( $\ell = 1, 2$ ) with energy  $E_i$ . The components  $\phi_{A\ell}(r)$  and  $\phi_{B\ell}(r)$  correspond, respectively, to the different sublattices  $A\ell$  and  $B\ell$  in each layer at the given valley ( $\tau = K, K'$ ).

In Fig. 7, we show the valley- and layer-resolved LDOS of the lowest-electron-energy states for both ring structures at  $B = 10$  T. In the case of isolated BLGR [Fig. 7(a)], for which the LDOS is computed in the energy range of  $[0, 0.2]$  eV, one can see that the LDOS of layer 1 (blue curves) is mostly centered inside the ring whereas in layer 2 the LDOS has its maximum value at the inner side of the ring. This behavior happens for both valleys,  $K$  and  $K'$  (solid and dashed curves, respectively). Besides, in each layer, the maximum contribution in the LDOS belongs to the  $K'$  valley. The lower panel of Fig. 7(a) shows the LDOS for each valley separately. We see that the LDOS contribution of the  $K'$  valley at the inner boundary of the ring is dominant which decreases with

radial distance and at the outer side of the ring, contributions of both valleys in the LDOS are almost equal. Shown in panel (b) of Fig. 7 is the LDOS of the hybrid BLGR. In this case, we compute the LDOS over the electron-energy states located between the lowest MLG LLs,  $n = 0$  and  $n = 1$ . Here too, the contribution of the  $K'$  valley in the LDOS is dominant in both layers. While the LDOS of the lower layer (blue curves) is centered in the middle of the ring, in the upper layer (red curves) the LDOS form rings with maximums at the inner and outer boundaries of the ring. Thus the difference between valley contributions as well as the layers ones in the LDOS at a given magnetic field can open up novel ways for applications of such graphene-based nanostructures in valleytronics.

#### IV. SUMMARY AND CONCLUDING REMARKS

In summary, based on continuum (Dirac-Weyl equation) and tight-binding models, we studied the electronic properties of BLGR, defined by IM potential, in two different configurations: an isolated BLGR and a hybrid one where a MLG ring is put on top of an infinite MLG sheet. By using the Dirac approximation and applying the IM boundary condition, we first obtained analytical results for the energy levels and corresponding wave spinors for both structures as function of a perpendicular magnetic field.

In contrast to the previously investigated zero-width BLGR, here, we predict a sizeable and magnetically tunable band gap for both ring structures which can be

measured by magnetotransport similar to the one performed recently for a MLG ring in Ref. [30]. We also showed that the presence of an interface boundary in a hybrid BLGR modifies drastically the energy levels as compared to that of an isolated BLGR. The energy spectrum of the isolated BLGR exhibits the intervalley symmetry  $E_e^K(m) = -E_h^{K'}(m)$  for electron (e) and hole (h) states, where  $m$  is the angular momentum quantum number and  $K, K'$  refer to the two valleys. This symmetry is broken in case of a hybrid BLGR. Further, the energy spectrum of both structures exhibits Aharonov-Bohm oscillations as the magnetic field varies. We confirmed the validity of our results by simulating the quantum rings by a staggered site-dependent potential in the TBM. We found good agreement between our analytical results obtained in the continuum approximation and those calculated within the TBM.

Finally, we analyzed the spatial dependence of the valley- and layer-resolved LDOS for the proposed BLGRs. Our findings are relevant for valleytronics applications.

Our results can be realized experimentally using different techniques such as magnetotransport measurements similar to those reported in Refs. [12, 30] for a MLG ring or using scanning probe techniques such as Scanning Tunneling Spectroscopy and Scanning Gate Microscopy [12] to probe the local density of states.

#### ACKNOWLEDGEMENTS

We gratefully acknowledge discussions with I. Snyman.

- 
- [1] Y.-W. Son, M. L. Cohen, and S. G. Louie, *Nature (London)* **444**, 347 (2006).
  - [2] M. Ezawa, *Phys. Rev. B* **73**, 045432 (2006).
  - [3] E. V. Castro, N. M. R. Peres, J. M. B. Lopes dos Santos, A. H. Castro Neto, and F. Guinea, *Phys. Rev. Lett.* **100**, 026802 (2008).
  - [4] T. S. Li, Y. C. Huang, S. C. Chang, Y. C. Chuang, and M. F. Lin, *Eur. Phys. J. B* **64**, 73 (2008).
  - [5] B. Sahu, H. Min, A. H. MacDonald, and S. K. Banerjee, *Phys. Rev. B* **78**, 045404 (2008).
  - [6] K.-T. Lam, C. Lee, and G. Liang, *Appl. Phys. Lett.* **95**, 143107 (2009).
  - [7] P. Recher, B. Trauzettel, A. Rycerz, Y. M. Blanter, C. W. J. Beenakker, and A. F. Morpurgo, *Phys. Rev. B* **76**, 235404 (2007).
  - [8] S. Russo, J. B. Oostinga, D. Wehenkel, H. B. Heersche, S. S. Sobhani, L. M. K. Vandersypen, and A. F. Morpurgo, *Phys. Rev. B* **77**, 085413 (2008).
  - [9] M. Huefner, F. Molitor, A. Jacobsen, A. Pioda, C. Stampfer, K. Ensslin, and T. Ihn, *Phys. Status Solidi B* **246**, 2756 (2009).
  - [10] M. Zarenia, J. M. Pereira, A. Chaves, F. M. Peeters, and G. A. Farias, *Phys. Rev. B* **81**, 045431 (2010).
  - [11] D. R. da Costa, A. Chaves, M. Zarenia, J. M. Pereira, Jr., G. A. Farias, and F. M. Peeters, *Phys. Rev. B* **89**, 075418 (2014).
  - [12] D. Cabosart, A. Felten, N. Reckinger, A. Iordanescu, S. Toussaint, S. Faniel, and B. Hackens, *Nano Lett.* **17**, 1344 (2017).
  - [13] M. Ezawa, *Phys. Rev. B* **76**, 245415 (2007).
  - [14] J. H. Bardarson, M. Titov, and P. W. Brouwer, *Phys. Rev. Lett.* **102**, 226803 (2009).
  - [15] M. Wimmer, A. R. Akhmerov, and F. Guinea, *Phys. Rev. B* **82**, 045409 (2010).
  - [16] G. Giavaras and F. Nori, *Appl. Phys. Lett.* **97**, 243106 (2010).
  - [17] A. V. Rozhkov, G. Giavaras, Y. P. Bliokh, V. Freilikher, and F. Nori, *Phys. Rep.* **503**, 77 (2011).
  - [18] M. T. Allen, J. Martin, and A. Yacoby, *Nat. Commun.* **3**, 934 (2012).
  - [19] D. P. Zebrowski, E. Wach, and B. Szafran, *Phys. Rev. B* **88**, 165405 (2013).
  - [20] A. D. Güçlü, P. Potasz, M. Korkusinski, P. Hawrylak, X. Li, S. P. Lau, L. Tang, R. Ji, and P. Yang, *Graphene Quantum Dots*, (Springer, Berlin, 2014).

- [21] D. Bischoff, A. Varlet, P. Simonet, M. Eich, H. C. Overweg, T. Ihn, and K. Ensslin, *Appl. Phys. Rev.* **2**, 31301 (2015).
- [22] D. Bischoff, M. Eich, O. Zilberberg, C. Rössler, T. Ihn, and K. Ensslin, *Nano Lett.* **15**, 6003 (2015).
- [23] M. Mirzakhani, M. Zarenia, D. R. da Costa, S. A. Ketabi, and F. M. Peeters, *Phys. Rev. B* **94**, 165423 (2016).
- [24] M. Mirzakhani, M. Zarenia, P. Vasilopoulos, and F. M. Peeters, *Phys. Rev. B* **95**, 155434 (2017).
- [25] M. Grüjić, M. Zarenia, A. Chaves, M. Tadić, G. A. Farias, and F. M. Peeters, *Phys. Rev. B* **84**, 205441 (2011).
- [26] T. G. Pedersen, C. Flindt, J. Pedersen, N. A. Mortensen, A.-P. Jauho, and K. Pedersen, *Phys. Rev. Lett.* **100**, 136804 (2008).
- [27] J. A. Fürst, J. G. Pedersen, C. Flindt, N. A. Mortensen, M. Brandbyge, T. G. Pedersen, and A.-P. Jauho, *New J. Phys.* **11**, 095020 (2009).
- [28] M. Kim, N. S. Safron, E. Han, M. S. Arnold, and P. Gopalan, *Nano Lett.* **10**, 1125 (2010).
- [29] J. G. Pedersen and T. G. Pedersen, *Phys. Rev. B* **85**, 035413 (2012).
- [30] B. S. Jessen, L. Gammelgaard, M. R. Thomsen, D. M. A. Mackenzie, J. D. Thomsen, J. M. Caridad, E. Duegaard, K. Watanabe, T. Taniguchi, T. J. Booth, T. G. Pedersen, A.P. Jauho, and P. Bøggild, *Nat. Nanotechnol.* **14**, 340 (2019).
- [31] W. Landgraf, S. Shallcross, K. Türschmann, D. Weckbecker, and O. Pankratov, *Phys. Rev. B* **87**, 075433 (2013).
- [32] E. Suárez Morell, R. Vergara, M. Pacheco, L. Brey, and Leonor Chico, *Phys. Rev. B* **89**, 205405 (2014).
- [33] E. S. Morell, P. Vargas, P. Häberle, Samuel A. Hevia, and Leonor Chico, *Phys. Rev. B* **91**, 035441 (2015).
- [34] M. Pelc, E. S. Morell, L. Brey, and L. Chico, *J. Phys. Chem. C* **119**, 10076 (2015).
- [35] M. Fleischmann, R. Gupta, D. Weckbecker, W. Landgraf, O. Pankratov, V. Meded, and S. Shallcross, *Phys. Rev. B* **97**, 205128 (2018).
- [36] A. Tiutiunnyka, C. A. Duqueb, F. J. Caro-Loperac, M. E. Mora-Ramosa, and J. D. Correac, *Physica E: Low-dimensional Systems and Nanostructures* **112**, 36 (2019).
- [37] M. Mirzakhani, F. M. Peeters, and M. Zarenia, *Phys. Rev. B* **101**, 075413 (2020).
- [38] J. Eroms and D. Weiss, *New J. Phys.* **11**, 095021 (2009).
- [39] T. Ihn, J. Güttinger, F. Molitor, S. Schnez, E. Schurtenberger, A. Jacobsen, S. Hellmüller, T. Frey, S. Dröscher, C. Stampfer, and K. Ensslin, *Mater. Today* **13**, 44 (2010).
- [40] L. A. Ponomarenko, F. Schedin, M. I. Katsnelson, R. Yang, E. H. Hill, K. S. Novoselov, and A. K. Geim, *Science* **320**, 356 (2008).
- [41] Q. Xu, M.-Y. Wu, G. F. Schneider, L. Houben, S. K. Malladi, C. Dekker, E. Yucelen, R. E. Dunin-Borkowski, and H. W. Zandbergen, *ACS Nano* **7**, 1566 (2013).
- [42] C.-J. Shih, A. Vijayaraghavan, R. Krishnan, R. Sharma, J.-H. Han, M.-H. Ham, Z. Jin, S. Lin, G. L. C. Paulus, N. F. Reuel, Q. H. Wang, D. Blankschtein, and M. S. Strano, *Nat. Nanotechnol.* **6**, 439 (2011).
- [43] G. Tsoukleri, J. Parthenios, C. Galiotis, and K. Papageelis, *2D Mater.* **2**, 024009 (2015).
- [44] D. G. Kvashnin, P. Vancsó, L. Y. Antipina, G. I. Márk, L. P. Biró, P. B. Sorokin, and L. A. Chernozatonskii, *Nano Research* **8**, 1250 (2015).
- [45] Thomas G. Pedersen, Christian Flindt, Jesper Pedersen, Antti-Pekka Jauho, Niels Asger Mortensen, and Kjeld Pedersen, *Phys. Rev. B* **77**, 245431 (2008).
- [46] Søren Schou Gregersen, Jesper Goor Pedersen, Stephen R. Power, and Antti-Pekka Jauho, *Phys. Rev. B* **91**, 115424 (2015).
- [47] M. R. Thomsen and T. G. Pedersen, *Phys. Rev. B* **95**, 235427 (2017).
- [48] Z. Liu, K. Suenaga, P. J. F. Harris, and S. Iijima, *Phys. Rev. Lett.* **102**, 015501 (2009).
- [49] D. Zhan, L. Liu, Y. N. Xu, Z. H. Ni, J. X. Yan, C. Zhao, and Z. X. Shen, *Sci. Rep.* **1**, 12 (2011).
- [50] Y. Kobayashi, K. I. Fukui, T. Enoki, K. Kusakabe, and Y. Kaburagi, *Phys. Rev. B* **71**, 193406 (2005).
- [51] Y. Niimi, T. Matsui, H. Kambara, K. Tagami, M. Tsukada, and H. Fukuyama, *Phys. Rev. B* **73**, 085421 (2006).
- [52] G. M. Rutter, J. N. Crain, N. P. Guisinger, P. N. First, and J. A. Stroscio, *J. Vac. Sci. Technology. A* **26**, 938 (2008).
- [53] K. W. Clark, X.-G. Zhang, G. Gu, J. Park, G. He, R. M. Feenstra, and A.-P. Li, *Phys. Rev. X* **4**, 011021 (2014).
- [54] W. Yan, S.-Y. Li, L.-J. Yin, J.-B. Qiao, J.-C. Nie, and L. He, *Phys. Rev. B* **93**, 195408 (2016).
- [55] C. P. Puls, N. E. Staley, and Y. Liu, *Phys. Rev. B* **79**, 235415 (2009).
- [56] T. Nakanishi, M. Koshino, and T. Ando, *Phys. Rev. B* **82**, 125428 (2010).
- [57] M. Koshino, T. Nakanishi, and T. Ando, *Phys. Rev. B* **82**, 205436 (2010).
- [58] J. Tian, Y. Jiang, I. Childres, H. Cao, J. Hu, and Y. P. Chen, *Phys. Rev. B* **88**, 125410 (2013).
- [59] H. M. Abdullah, M. Zarenia, H. Bahlouli, F. M. Peeters, and B. Van Duppen, *EPL* **113**, 17006 (2016).
- [60] L.-J. Yin, K.-K. Bai, W.-X. Wang, S.-Y. Li, Y. Zhang, and L. He, *Front. Phys.* **12**, 127208 (2017).
- [61] M. Mirzakhani, M. Zarenia, and F. M. Peeters, *J. Appl. Phys* **123**, 204301 (2018).
- [62] D. Yin, W. Liu, X. Li, L. Geng, X. Wang, and P. Huai, *Appl. Phys. Lett.* **103**, 173519 (2013).
- [63] M. Mirzakhani, M. Zarenia, P. Vasilopoulos, S. A. Ketabi, and F. M. Peeters, *Phys. Rev. B* **96**, 125430 (2017).
- [64] M. Mirzakhani, M. Zarenia, S. A. Ketabi, D. R. da Costa, and F. M. Peeters, *Phys. Rev. B* **93**, 165410 (2016).
- [65] M. V. Berry and R. J. Modragon, *Proc. R. Soc. London A* **412**, 53 (1987).
- [66] S. Schnez, K. Ensslin, M. Sigrist, T. Ihn, *Phys. Rev. B* **78** 195427 (2008).
- [67] D. R. da Costa, M. Zarenia, A. Chaves, G. A. Farias, and F. M. Peeters, *Carbon* **78**, 392 (2014).
- [68] M. Zarenia, J. M. Pereira, Jr., F. M. Peeters, and G. A. Farias, *Nano Lett.* **9**, 4088 (2009).
- [69] M. Zarenia, J. M. Pereira, A. Chaves, F. M. Peeters, and G. A. Farias, *Phys. Rev. B* **81**, 045431 (2010); *ibid.* **82**, 119906 (2010).
- [70] G. Giovannetti, P. A. Khomyakov, G. Brocks, P. J. Kelly, and J. van den Brink, *Phys. Rev. B* **76**, 073103 (2007); B. Sachs, T. O. Wehling, M. I. Katsnelson, and A. I. Lichtenstein, *ibid.* **84**, 195414 (2011).
- [71] S. Bhowmick, A. K. Singh, and B. I. Yakobson, *J. Phys. Chem. C* **115**, 9889 (2011).
- [72] E. McCann and V. I. Fal'ko, *Phys. Rev. Lett.* **96**, 086805 (2006).
- [73] J. Nilsson, A. H. Castro Neto, N. M. R. Peres, and F. Guinea, *Phys. Rev. B* **73**, 214418 (2006).

- [74] E. McCann, Phys. Rev. B **74**, 161403(R) (2006)
- [75] R. Peierls, Z. Phys. **80**, 763 (1933).
- [76] T. G. Pedersen Phys. Rev. B **96**, 115432 (2017).
- [77] D. R. da Costa, M. Zarenia, A. Chaves, G. A. Farias, and F. M. Peeters Phys. Rev. B **93**, 085401 (2016).
- [78] Y. Aharonov and D. Bohm, Phys. Rev. **115**, 485 (1959).
- [79] R. A. Webb, S. Washburn, C. P. Umbach and R. B. Laibowitz, Phys. Rev. Lett. **54** 2696 (1985).
- [80] T. Chakraborty and P. Pietiläinen, Phys. Rev. B **50**, 8460 (1994).
- [81] J. Wurm, M. Wimmer, H. U. Baranger and K. Richter, Semicond. Sci. Technol. **25** 034003 (2010).
- [82] J. Schelter, D. Bohr, and B. Trauzettel, Phys. Rev. B **81**, 195441 (2010).